

See discussions, stats, and author profiles for this publication at: <https://www.researchgate.net/publication/255756132>

# Switching of interfacial instabilities from the liquid/air interface to the liquid/liquid interface in a polymer bilayer

ARTICLE *in* SOFT MATTER · SEPTEMBER 2011

Impact Factor: 4.03 · DOI: 10.1039/C1SM05370A

---

CITATIONS

5

---

READS

23

## 4 AUTHORS, INCLUDING:



Lin Xu

University of Minho

15 PUBLICATIONS 136 CITATIONS

SEE PROFILE



Dipankar Bandyopadhyay

Indian Institute of Technology Guwahati

59 PUBLICATIONS 534 CITATIONS

SEE PROFILE



Ashutosh Sharma IITK

Indian Institute of Technology Kanpur

334 PUBLICATIONS 7,407 CITATIONS

SEE PROFILE

Cite this: *Soft Matter*, 2011, **7**, 8056

www.rsc.org/softmatter

PAPER

# Switching of interfacial instabilities from the liquid/air interface to the liquid/liquid interface in a polymer bilayer

Lin Xu,<sup>a</sup> Dipankar Bandyopadhyay,<sup>b</sup> Ashutosh Sharma<sup>\*ac</sup> and Sang Woo Joo<sup>\*a</sup>

Received 3rd March 2011, Accepted 31st May 2011

DOI: 10.1039/c1sm05370a

A combined experimental and theoretical study uncovers the interfacial morphologies of a thin bilayer composed of a polystyrene (PS) upper layer and a poly-methylmethacrylate (PMMA) lower layer, coated on a Si wafer with 120 nm oxide layer. The bilayers with ultrathin PMMA layer ( $M_w = 15 \text{ kg mol}^{-1}$  and  $365 \text{ kg mol}^{-1}$ ) under a thin PS ( $M_w = 2.5 \text{ kg mol}^{-1}$ ) layer are always found to evolve with a strongly deforming polymer/air interface over a non-deforming polymer/polymer interface. In contrast, the polymer/polymer interface is found to deform more when the PMMA layer is lower viscosity ( $M_w = 15 \text{ kg mol}^{-1}$ ) and thicker. With the increase in the  $M_w$  of PS films, the bilayers also show larger deformability of the polymer/polymer interface. The linear stability analysis and nonlinear simulations confirm that the increase (decrease) in the viscous resistance due to the larger (smaller) molecular weight and smaller (larger) thickness of the PMMA layer enforces lesser (bigger) deformability in the polymer/polymer interface. The computations mimicking the experiments are presented to demonstrate the switchover of the dominant mode of instability from the polymer/air to polymer/polymer interface varying the thickness of the lower layer and the viscosity of both PS and PMMA layers.

## 1. Introduction

The spinodal<sup>1–29</sup> and defect-induced<sup>30–41</sup> instabilities of thin polymer films have been studied in recent times because their frequent appearance in the cutting-edge technological products and processes, which includes coatings of functional materials, high precision sensors, patterns on solar panels, fuel cell electrodes, smart adhesives, optoelectronic devices, biological membranes, micro/nano fluidic devices, and components of drug delivery modules.<sup>42–46</sup> Self-organizing ultrathin films are also found to be the model mesoscale prototypes to study different facets of basic science, namely, intermolecular forces, meso-dewetting, adhesion and phase transition.<sup>1–29,47–51</sup> Even though intense research efforts over past few decades have improved the understanding on the instabilities of thin polymer films, plenty of questions are still found to be unresolved.<sup>2,7</sup>

Dewetting of an ultrathin polymer films on a homogeneous surface is among the most deeply studied systems,<sup>1–29</sup> which initiates with the formation of randomly placed holes in the films. The holes grow in time and form ribbon-like structures, which further break up into a collection of droplets. In contrast to the

single film scenario, the dewetting of ultrathin polymer bilayers is more complex and interesting because it grows by simultaneous deformations of the coupled polymer/air and polymer/polymer interfaces. Fig. 1 schematically shows a thin polymer bilayer resting on a solid substrate. Previous studies<sup>52–87</sup> indicate that the bilayer dewetting has distinct advantages over single layers in fabricating self-organized embedded/encapsulated micro/nano structures and in miniaturization of the dewetted patterns. Thus far, the spinodal,<sup>63,64,68,71–79,82</sup> marangoni<sup>71–73,83–85</sup> and defect-induced<sup>80,81</sup> instabilities of ultrathin polymer bilayers composed of viscous,<sup>63,64,68,71–85</sup> viscoelastic,<sup>69,86,87</sup> and composite<sup>86,87</sup> films have been explored. Importantly, many of these experimental<sup>64</sup>

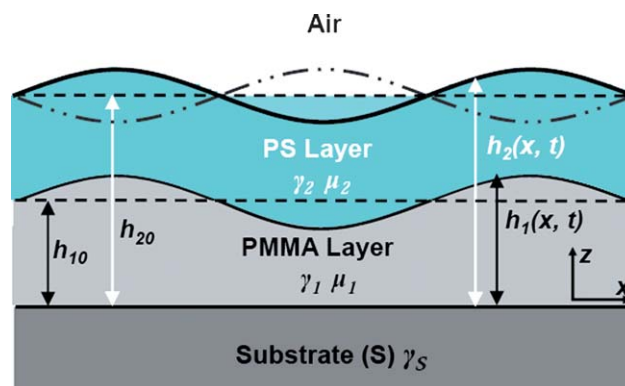


Fig. 1 A schematic diagram of our chosen polymer bilayer system.

<sup>a</sup>School of Mechanical Engineering, Yeungnam University Gyongsan, 712-749, South Korea. E-mail: ashutos@iitk.ac.in; swjoo@yu.ac.kr

<sup>b</sup>Department of Chemical Engineering, Indian Institute of Technology Guwahati, 781039, India

<sup>c</sup>Department of Chemical Engineering, Indian Institute of Technology, Kanpur, 208016, India

and theoretical<sup>74,77–79</sup> works underline the importance of the viscosity contrast in the polymer layers of a bilayer in changing the kinetics of dewetting and subsequent interfacial morphologies. In general, the viscous influences in films can be altered by changing the dynamic viscosity of the films or by reducing the influence of the bounding substrate by increasing the thickness of the films. Interestingly, for ultrathin films, changing film thickness also alters the magnitude of the intermolecular interaction. Thus, interplay between the kinetic and thermodynamic forces is expected to prevail in the spatiotemporal dynamics of these systems. Previous literature suggests that there are quite a few unresolved issues involving kinetically and thermodynamically controlled bilayer dewetting. Especially, the relative amplitude of deformations at the polymer/air and polymer/polymer interfaces and the subsequent interfacial morphologies with the change in the dynamic viscosities and film thickness of the films is still among the intriguing open questions.

In this paper, the interfacial morphologies of a dewetting bilayer (Fig. 1) with sharp viscosity contrast among the films are studied. The bilayer is composed of polystyrene (PS) upper layer and poly(methyl methacrylate) (PMMA) lower layer and resting on silicon (Si) wafer with 120 nm oxide layer. In experiments, the molecular weight of the polymers is varied to alter the viscosity of the films. The study shows that by changing the viscosity and thickness of the polymer films, the dominant mode for instability can be shifted from the polymer/polymer interface to the polymer/air interfaces or *vice versa*. With the help of systematic experiments the absolute deformations at the polymer/air and the polymer/polymer interfaces are obtained and by comparing them the location of the dominant mode of instability is identified. A long-wave linear stability analysis (LSA) uncovers that the change in the viscous resistance because of the change in the dynamic viscosity of the films and the film thicknesses are the major reasons behind this switchover. Nonlinear simulations are performed under experimental conditions to mimic the experimentally obtained interfacial morphologies at the polymer/air and polymer/polymer interfaces.

## 2. Experimental procedure

The system under investigation is a polymeric bilayer of polystyrene (PS,  $M_w = 2.5 \text{ kg mol}^{-1}$ ,  $4.1 \text{ kg mol}^{-1}$ ,  $M_w = 22 \text{ kg mol}^{-1}$  and  $M_w = 44 \text{ kg mol}^{-1}$ ;  $M_w/M_n < 1.1$ ) and poly-(methyl methacrylate) (PMMA,  $M_w = 15 \text{ kg mol}^{-1}$ , and  $365 \text{ kg mol}^{-1}$ ;  $M_w/M_n < 3$ ) on the Si wafer with 120 nm oxide layer. PMMA films were spin coated from a 1,2-dichloroethane solution onto the Si wafer. The bilayer films were prepared by spin coating the cyclohexane solution of PS on the PMMA films. The thickness of the films was measured by ellipsometry. To initiate the dewetting process, the samples were heated to a temperature ( $160^\circ\text{C}$ ) well above the glass transition temperature of PS and PMMA under the air. The surface morphology was observed by optical microscopy (OM) in the reflection mode at annealing temperature and atomic force microscopy (AFM) operating in the tapping mode at room temperature. The spring constant of the cantilever in the AFM is  $2 \text{ N m}^{-1}$ . The cantilever is oscillated close to its resonance frequency between 65 and 75 kHz. The PS upper layer was removed by immersing the samples in cyclohexane. Previous

studies<sup>64</sup> have shown that removal of PS employing cyclohexane did not influence the morphology of the PMMA layer. After drying, the remaining PMMA surface was imaged to obtain the morphology of the PS/PMMA interface. The receding contact angles of PS on the PMMA lower layer are obtained from the profile images of the rim.

## 3. Problem formulation

### A. Nonlinear evolution equations

The evolution equations for the polymer/air and polymer/polymer interfaces are derived assuming the films to be incompressible, isothermal and with constant physical properties. Since the experimental studies are done well above the glass transition temperatures of the polymers, the layers are assumed to behave like a Newtonian fluid. Owing to the small thicknesses of the films (i) the body forces due to the intermolecular interactions are assumed to be much larger the gravitational force and (ii) the inertial terms are neglected from the equations of motion assuming laminar flow in the Stokes regime. The equations are derived with  $x$  as the coordinate parallel and  $z$  as the coordinate normal to the substrate surface as schematically shown in the Fig. 1. In the following equations, for the layer  $i$  (the subscripts  $i = 1$  and 2 represent upper and lower layer or interface)  $u_i$  and  $w_i$  are the  $x$ - and  $z$ -components of velocity,  $\mu_i$  is the dynamic viscosity,  $\rho_i$  is the density,  $\pi_i$  is the excess intermolecular force,  $p_i$  is the isotropic static pressure in the liquid,  $P_i (= p_i - \pi_i)$  is the total pressure, and  $\gamma_i$  is the surface tension. The symbol  $\gamma_s$  represents the surface energy of the solid substrate. The subscripts  $x$ ,  $z$  and  $t$  shown in the governing equations and boundary conditions denote differentiation with respect to the respective variable. The notations  $h_1$  and  $h_2$  represent lower layer thickness and the combined thickness of the upper and the lower layer, respectively. The parameters with subscript zero represent the respective base state thicknesses of the films. For the two layers, the equations of motion under the long-wave approximation,  $\mu_i u_{izz} = (p_i + \phi_i)_x$ , the equations of continuity for incompressible fluids,  $u_{ix} + w_{iz} = 0$ , and the kinematic equations  $h_{it} + u_i|_{at h_i} h_{ix} = w_i|_{at h_i}$  leads to the following evolution equations:<sup>71–85</sup>

$$h_{1t} - \frac{1}{3\mu_1} [h_1^3 P_{1x}]_x + \frac{1}{2\mu_1} [h_1^2 (h_1 - h_2) P_{2x}]_x = 0, \quad (1)$$

$$h_{2t} + \left[ \left\{ \frac{1}{3\mu_2} (h_1 - h_2)^3 + \frac{1}{\mu_1} (h_1 - h_2) h_1 \left( h_2 - \frac{h_1}{2} \right) \right\} P_{2x} \right]_x + \frac{1}{2\mu_1} \left[ h_1^2 \left( \frac{h_1}{3} - h_2 \right) P_{1x} \right]_x = 0. \quad (2)$$

The boundary conditions employed are: (i) at  $z = h_2$ , shear-free boundary ( $\mu_2 u_{2z} = 0$ ); (ii) at  $z = h_1$ , continuity of velocities ( $u_2 = u_1$ , and  $w_2 = w_1$ ), and shear-stress balance ( $\mu_2 u_{2z} = \mu_1 u_{1z}$ ); (iii) at  $z = 0$ , no slip and impermeability ( $u_1 = w_1 = 0$ ). The pressures at the interfaces are derived from the normal stress balances at the interfaces,  $P_1 = p_1 + \phi_1 = p_2 - \gamma_{21} \nabla^2 h_1 - \pi_1$  and  $P_2 = p_2 + \phi_2 = p_0 - \gamma_2 \nabla^2 h_2 - \pi_2$ . Here  $p_0$  is the ambient gas pressure and  $\gamma_{21}$  is the interfacial tension at the polymer/polymer interface. The expressions for the intermolecular interaction arising from the van der Waals forces are:<sup>77–79</sup>

$$\pi_1 = \frac{2d_0^2 S_{1S2}}{h_1^3} + \frac{2d_0^2 (S_{1S} - S_{1S2})}{(h_1 + h_3)^3} + \frac{3B_1}{h_1^4}, \quad (3)$$

$$\pi_2 = \frac{2d_0^2 S_{21}}{h_3^3} + \frac{2d_0^2 (S_{1S} - S_{1S2})}{(h_1 + h_3)^3} + \frac{3B_2}{h_3^4}. \quad (4)$$

Here  $d_0$  ( $\sim 0.158$  nm) is the van der Waals equilibrium distance between the two surfaces/interfaces,  $S_{ijk}(= \gamma_{jk} - \gamma_{ik} - \gamma_{ij})$  denote the spreading coefficient of material  $i$  resting on material  $j$  and bounded by  $k$ ,  $\gamma_{ij}$  is the interfacial tensions ( $s, l$  and  $2$ ).<sup>88,89</sup> The expressions for Hamaker constants ( $A_i$ ) in terms of the spreading coefficients are,  $A_{22} - A_{12} = -12\pi d_0^2 S_{21}$ ,  $A_{11} + A_{s2} - A_{s1} - A_{12} = -12\pi d_0^2 S_{1S2}$ , and  $A_{s2} - A_{12} = -12\pi d_0^2 (S_{1S2} - S_{1S})$ .<sup>88,89</sup> In general, a negative (positive) equilibrium spreading coefficient (effective Hamaker constant) signifies instability. The Born-repulsion terms  $B_i$ , remove the contact line singularity, are obtained by finding out the free energy minimum at a cut-off precursor thickness of  $l_0$ ,  $\pi_1(l_0) = 0$  and  $\pi_2(l_0) = 0$ .

### B. Linear stability analysis

The evolution equations are linearized employing the normal linear modes ( $h_i = h_{i0} + \varepsilon e^{\omega t + ikx}$ ) and the following dispersion relation is obtained:<sup>77,78</sup>

$$\omega = \left[ -(B + C) \pm \sqrt{(B - C)^2 + 4AD} \right] / 2, \quad (5)$$

where

$$A = [(h_{10}^3/3\mu_1)(\gamma_2 k^4 - k^2 \pi_{1h_2})] + [(1/2\mu_1)(h_{20} - h_{10})h_{10}^2(\gamma_2 k^4 - k^2 \pi_{2h_2})],$$

$$B = [(h_{10}^3/3\mu_1)(\gamma_{21} k^4 - k^2 \pi_{1h_1})] - [(1/2\mu_1)(h_{20} - h_{10})h_{10}^2(k^2 \pi_{2h_1})],$$

$$C = [(1/2\mu_1)h_{10}^2(h_{20} - h_{10}/3)(\gamma_2 k^4 - k^2 \pi_{1h_2})] + [(1/3\mu_2)(h_{20} - h_{10})^3 + (1/\mu_1)h_{10}(h_{20} - h_{10})(h_{20} - h_{10}/2)](\gamma_2 k^4 - k^2 \pi_{2h_2}),$$

$$D = [(1/2\mu_1)h_{10}^2(h_{20} - h_{10}/3)(\gamma_{21} k^4 - k^2 \pi_{1h_1})] - [(1/3\mu_2)(h_{20} - h_{10})^3 + (1/\mu_1)h_{10}(h_{20} - h_{10})(h_{20} - h_{10}/2)](k^2 \pi_{2h_1}).$$

Here the gradients of the disjoining pressures,  $\pi_{jh,l} = (\partial \pi_j / \partial h_i)$  where  $j$  and  $i$  are indices representing 1 or 2.

### C. Non-dimensional form

Eqn (1) and (2) are made dimensionless by introducing the following set of variables:  $X = K_1(x/h_{10})$ ;  $T = K_2(\nu_1/h_{10}^2)$ ;  $H_1 = h_1/h_{10}$ ;  $H_2 = h_2/h_{10}$ ;  $d = d_0/h_{10}$ ;  $l = l_0/h_{10}$ ;  $M = \gamma_2/\gamma_{21}$ ;  $R = \mu_1/\mu_2$ . The terms  $K_1 = (BC)^{1/2}$  and  $K_2 = B^2C$  where  $B = (2d^2[S_{1S2}]/3\rho_1\nu_1^2)$ ,  $C = 3\rho_1\nu_1^2/\gamma_{12}h_{10}$  and  $\nu_1 = \mu_1/\rho_1$ . The dimensionless equations thus obtained for the interfaces are:<sup>77-79</sup>

$$H_{1T} + [H_1^3 \{ MH_{2XX} + H_{1XX} + [(1/H_1^3) + (N-1)/H_2^3 + B_1^N] \}_X]_X + (3/2)[H_1^2(H_2 - H_1) \{ MH_{2XX} + [P/(H_2 - H_1)^3 + (N-1)/H_2^3 + B_2^N] \}_X]_X = 0, \quad (6)$$

$$H_{2T} + [\{ R(H_2 - H_1)^3 + 3(H_2 - H_1)H_1(H_2 - H_1/2) \} \{ MH_{2XX} + [P/(H_2 - H_1)^3 + (N-1)/H_2^3 + B_2^N] \}_X]_X + (3/2)[H_1^2(H_2 - H_1/3) \{ MH_{2XX} + H_{1XX} + [1/H_1^3 + (N-1)/H_2^3 + B_1^N] \}_X]_X = 0. \quad (7)$$

where the dimensionless terms,  $B_1^N = [l/H_1^4] + [N-1]l^4/[(H_2 - H_1 + l)^3 H_1^4]$  and  $B_2^N = [lP/(H_2 - H_1)^4] + [N-1]l^4/[(H_1 + l)^3(H_2 - H_1)^4]$ . Eqn (6) and (7) were discretized in space employing a central difference scheme with a half node interpolation. The sets of ordinary differential equations (ODEs) thus obtained were time marched employing Gear's algorithm. The simulations were initiated with a volume preserving infinitesimal random perturbation at the interfaces. Periodic boundary conditions were enforced at the spatial boundaries. The grid independence of the solutions was verified to ensure the correctness of the results.

## 4. Results and discussion

The instabilities in ultrathin bilayers are in general governed by the thermodynamic forces when the films are of similar viscosity. The attractive intermolecular interactions destabilize the bilayer films whereas the repulsive intermolecular interactions and the surface tensions at the interfaces always stabilize the layers. In such situations dewetted morphologies are thermodynamically governed. However, in a bilayer configuration it is always difficult to maintain a similar viscosity at the layers and bilayers with dissimilar viscosity is a most commonly encountered system in the experiments. Importantly, when the films have considerably different viscosities, the relative viscous resistance at the films can significantly alter the force field governed by the thermodynamics of the system and the instability can become a kinetically controlled one. A larger viscous resistance in a film can reduce its deformability because of the destabilizing intermolecular interaction, which can lead to an entirely different interfacial morphologies as shown briefly in some of the previous studies.<sup>64,78,79</sup>

Fig. 1 shows a schematic diagram of the PS/PMMA bilayer resting on a solid substrate. In the experiments the bilayer is placed on the Si wafer with thick oxide layer, where the lower layer (PMMA) is spinodally stable regardless of its thickness and does not undergo dewetting by hole formation. To demonstrate the key features of the kinetically controlled bilayer dewetting, the PS upper layer is kept at constant thickness ( $65 \pm 3$  nm) and of low molecular weight ( $M_w = 2.5$  kg mol<sup>-1</sup> to  $M_w = 44$  kg mol<sup>-1</sup>), which ensures that the PS layer always rupture and dewet on the PMMA layer. The low molecular weight PMMA ( $M_w = 15$  kg mol<sup>-1</sup>,  $\mu_1 = 2.92 \times 10^5$  Pa s at 160 °C)<sup>90</sup> at 160 °C behaves like a viscous liquid and can deform during the dewetting process. However, the higher molecular weight PMMA ( $M_w = 365$  kg mol<sup>-1</sup>,  $\mu_1 = 1.50 \times 10^{10}$  Pa s at 160 °C)<sup>90</sup> at 160 °C behaves more like a solid surface under a dewetting PS layer.

Fig. 2 describes the results with a highly viscous PMMA ( $M_w = 15$  kg mol<sup>-1</sup>) layer under a PS ( $M_w = 2.5$  kg mol<sup>-1</sup>) layer with much lower viscosity. Fig. 2a–2c (2d–2f) show the optical



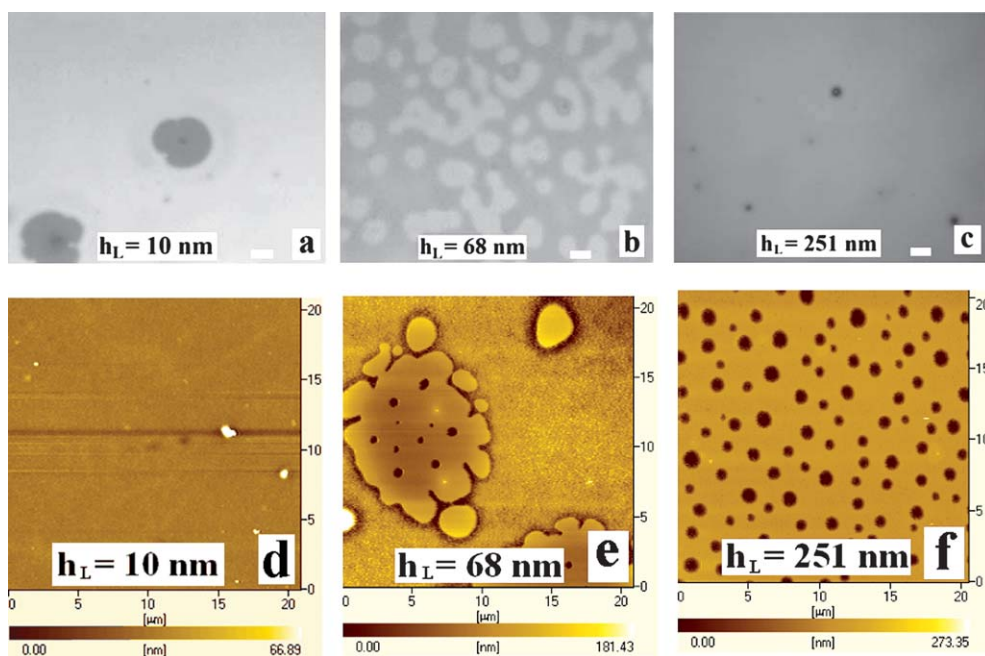
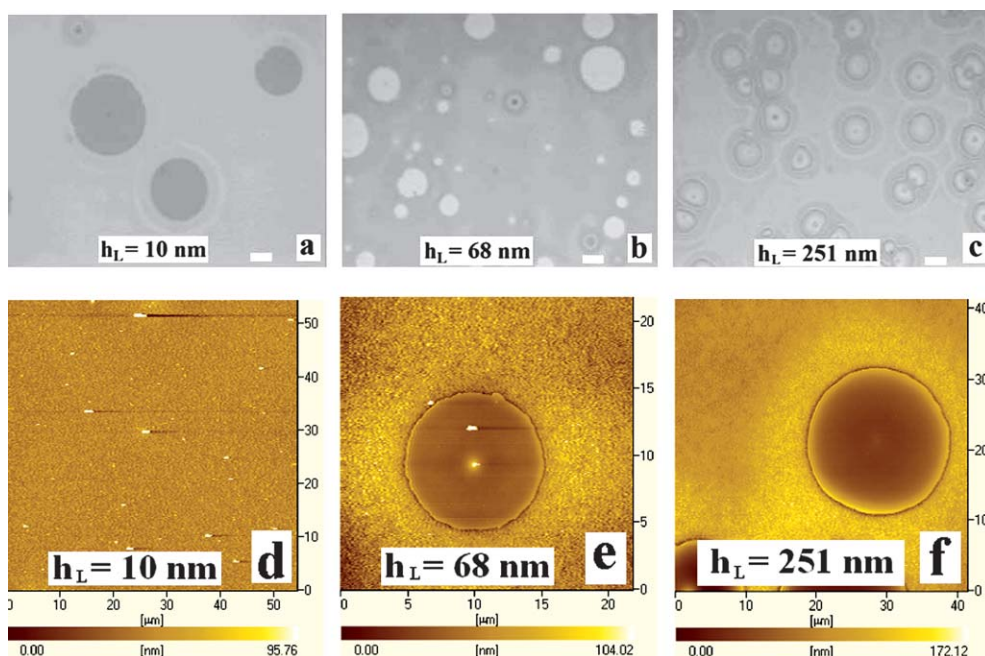


**Fig. 2** The PS ( $M_w = 2.5 \text{ kg mol}^{-1}$ ,  $h_U = 65 \pm 3 \text{ nm}$ ) film/the PMMA film ( $M_w = 15 \text{ kg mol}^{-1}$ , different film thickness)/the Si wafer with 120 nm oxide layer was treated at 160 °C. (a)–(c) a series of OM images show the morphology of the liquid-gas interface; (d)–(f) a series of AFM images show the morphology of the polymer/polymer interface after the PS upper layer is removed. The scale of bar in (a)–(c) is 10  $\mu\text{m}$ .

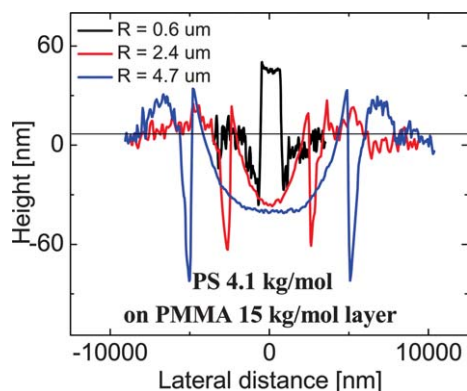
micrographs (AFM images) for the polymer/air (polymer/polymer–PS/PMMA) interface. Fig. 2a shows that the PS/PMMA interface cannot deform when the PMMA layer is thin. The dewetting pathway shown here is similar to the single film dewetting where the polymer/air deforms to form holes in the PS film (Fig. 2a and 2d). However, at intermediate thicknesses the interfaces are found to evolve in two different wavelengths as shown in the images (b) and (e). In such situation two simultaneous things happen. Firstly, with the increase in the film thickness of the PMMA layer the viscous resistance at the PMMA layer reduces, which allows the PS layer to penetrate into the PMMA layer after its rupture. The signature of the penetration of PS layer near the contact line of the holes formed can be observed in the AFM image Fig. 2e. Secondly, the dark spots in the AFM image also confirm the presence of a secondary instability where the PS layer locally invades into the PMMA layer. The distance between these local invasions of the PS layer are found to be much smaller than the wavelength of PS dewetting on the PMMA layer. When the thickness of the PMMA layer is further increased, the lesser viscous resistance at the PMMA layer further increases the deformability of the PS/PMMA interface and the instability evolves by larger deformation of the polymer/polymer interface as compared to the polymer/air interface (Fig. 2c and 2f). Fig. 2 clearly depicts that the variation in the viscous dissipation and the strength of intermolecular forces due to the change in the thickness of the PMMA layer plays a crucial role in switching the dominant mode of instability from once interface to the other. Later mimicking the experiments we have qualitatively explained the switchover of the dominant mode through simulations.

Fig. 3 shows a similar case as Fig. 2 but here the PS ( $M_w = 4.1 \text{ kg mol}^{-1}$ ) layer is of higher viscosity. Fig. 3a–3c confirm that with

increase in the film thickness of the PMMA layer, the polymer/air interface is always unstable. Fig. 3d–3f show that the PS layer penetrates into the thicker PMMA films near the contact line whereas the PS/PMMA interface remains literally unreformed when the PMMA layer is very thin. Fig. 4 shows the profile images of hole on a thick PMMA layer with different hole-radii after removing the PS layer. Fig. 4 clearly depicts that when the PMMA layer is thick enough the instability at the polymer/polymer interface starts with a larger deformation towards the polymer/air interface, which forms holes at the PS layer. Thereafter, when the hole grows to achieve equilibrium contact angle the three-phase contact line penetrates into the PMMA layer and forms trenches. Fig. 5 and 6 together show that with increase in the PS molecular weight ( $M_w = 22 \text{ kg mol}^{-1}$  and  $44 \text{ kg mol}^{-1}$ ) the interfacial morphologies remain similar to as shown in the Fig. 3 and 4. Fig. 7 shows that when the PMMA viscosity is increased by increasing its molecular weight ( $M_w = 365 \text{ kg mol}^{-1}$ ) the instability is always evolved by stronger deformation at the polymer/air interface. The AFM images shown in Fig. 8 confirm that the PS/PMMA interface hardly deforms in such cases. The interfacial profiles of the polymer/air interface shown in the Fig. 9a and 9b more clearly demonstrates that how the morphology of the rim changes as the dynamic viscosity of the upper layer is increased by increasing the molecular weight. These two plots also show that the change in the receding contact angle  $\theta$  of PS on a non-deforming PMMA layer ( $10 \pm 1^\circ$ ) as shown in Fig. 9c. From Fig. 9c, it is found that the receding contact angle  $\theta$  of PS ( $M_w = 2.5 \text{ kg mol}^{-1}$ ) on the PMMA lower layer is obviously smaller than that in other three cases. With the increase in the viscosities of PS upper layer, the wavelength of interfacial instability can be influenced, which may be the major reason of the change of the receding contact



**Fig. 3** The PS ( $M_w = 4.1 \text{ kg mol}^{-1}$ ,  $h_U = 65 \pm 3 \text{ nm}$ ) film/the PMMA film ( $M_w = 15 \text{ kg mol}^{-1}$ , different film thickness)/the Si wafer with 120 nm oxide layer was treated at  $160^\circ\text{C}$ . (a)–(c) a series of OM images show the morphology of the liquid-gas interface; (d)–(f) a series of AFM images show the morphology of the polymer/polymer interface after the PS upper layer is removed. The scale of bar in (a)–(c) is  $10 \mu\text{m}$ .



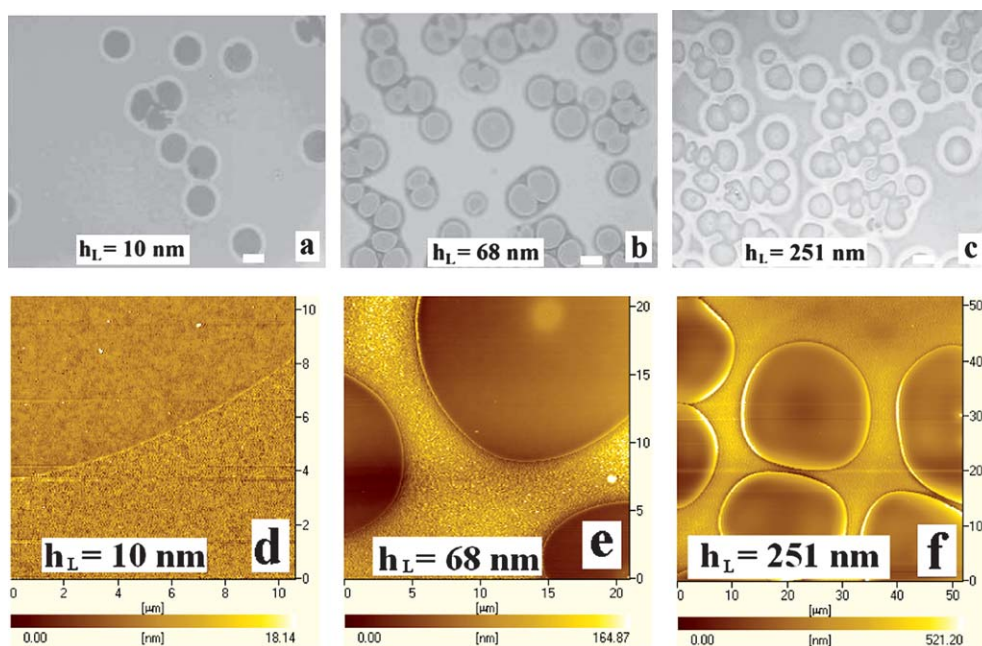
**Fig. 4** The profile images of hole with different hole radius after removing the PS layer: PS film ( $M_w = 4.1 \text{ kg mol}^{-1}$ ,  $h_U = 65 \pm 3 \text{ nm}$ ) on the PMMA film ( $M_w = 15 \text{ kg mol}^{-1}$ , the film thickness  $h_L = 251 \text{ nm}$ ). The  $R$  in Figure 4 is the radius of the holes.

angle. Our simulation results also show the change of the wavelength of interfacial instability with the ratio of viscosities of the films. In following part, we will show the simulation results in detail.

To describe the experimental results a brief computational study has been performed and the results are shown in the Fig. 10 to 12. The parameters chosen for the computations are within the range of the experimental conditions as can be found in the figure captions. The experiments clearly suggest that the dewetting and the subsequent interfacial morphologies of ultrathin bilayers are dictated by the location of the dominant mode. The lower layer rupture can be envisaged as larger deformation at the polymer/polymer interface towards the substrate as compared to the

polymer/air interface. In such a scenario the dominant mode of instability is expected to be located at the polymer/polymer interface. The possibility of the upper layer rupture appears when either the polymer/polymer interface deforms more towards the polymer/air interface or *vice versa*.

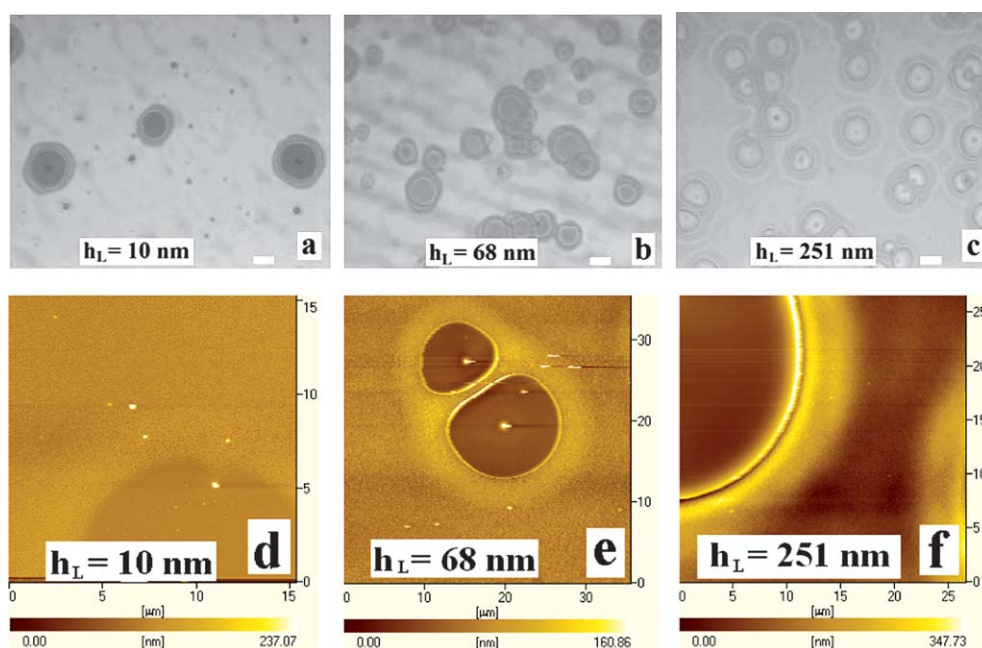
The results obtained from the LSA are shown in the Fig. 10 and 11. The surface energies of the PS ( $= 40 \text{ mN m}^{-1}$ ) and PMMA ( $30 \text{ mN m}^{-1}$ ) layers are kept constant and the substrate surface energies are varied from  $20 \text{ mN m}^{-1}$  to  $120 \text{ mN m}^{-1}$  to discuss the cases with thermodynamically stable ( $20 \text{ mN m}^{-1}$ ) and unstable ( $40 \text{ mN m}^{-1}$ ,  $60 \text{ mN m}^{-1}$  and  $120 \text{ mN m}^{-1}$ ) lower film. To mimic the experiments the thermodynamically unstable lower films are made kinetically stable by increasing the viscosities. Fig. 10 shows a bimodal nature of the growth coefficient ( $\omega$ ) vs. wavenumber ( $k$ ) plots with a pair of maxima. The larger wavenumber maximum corresponds to the polymer/polymer interface owing to the smaller stabilizing interfacial tension whereas the smaller wavenumber maximum depicts the growth rate of the polymer/air interface having larger surface tension. Fig. 10a shows that when the lower layer is extremely thin (curve 1) the instability is dictated by the larger wavenumber maxima, which signifies that the dominant mode of instability is at the polymer/polymer interface and rupture of the lower layer. Curves 1–3 suggests that as the lower layer thickness is progressively increased the dominant mode shifts from the larger wavenumber maximum to the smaller wavenumber maximum. Importantly, the shift of the dominant growth coefficient ( $\omega_m$ ) from one maximum to the other can be attributed to the shift of dominant mode from the polymer/polymer interface (larger wavenumber maxima) to the polymer/air interface (smaller wavenumber maxima). The shift also signifies that now the instability evolves by the first rupture of the upper layer with larger deformation



**Fig. 5** The PS ( $M_w = 22 \text{ kg mol}^{-1}$ ,  $h_U = 65 \pm 3 \text{ nm}$ ) film/the PMMA film ( $M_w = 15 \text{ kg mol}^{-1}$ , different film thickness)/the Si wafer with 120 nm oxide layer was treated at  $160^\circ\text{C}$ . (a)–(c) a series of OM images show the morphology of the liquid-gas interface; (d)–(f) a series of AFM images show the morphology of the polymer/polymer interface after the PS upper layer is removed. The scale of bar in (a)–(c) is  $10 \mu\text{m}$ .

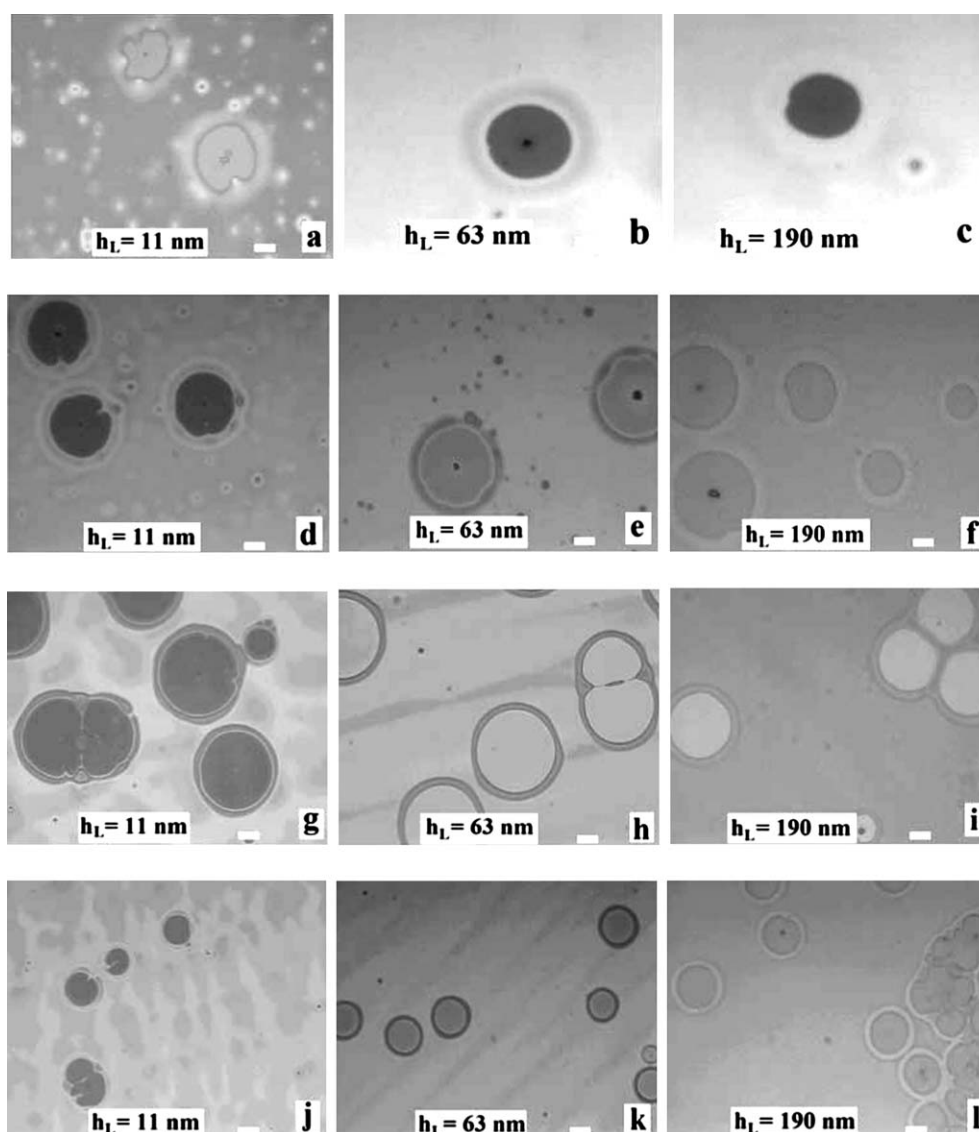
at the polymer/air interface. Curves 3 and 4 in Fig. 10a show that with increase in the lower layer thickness the viscous resistance at the polymer/polymer interface reduced and a larger deformability of the interface shifts the dominant mode again back to the polymer/polymer interface. However, in this situation the instability grows by the rupture of the upper layer.

Fig. 10c and 10d show the variations of  $\omega_m$  and the corresponding wavelength ( $\lambda_m$ ) when the lower layer thickness is varied. Curve 1 in Fig. 10c and 10d shows a typical situation where the lower layer is thermodynamically stable and the upper layer is unstable. Thus, for the bilayers with ultrathin lower layers, the instability is dictated by the deformation of the



**Fig. 6** The PS ( $M_w = 44 \text{ kg mol}^{-1}$ ,  $h_U = 65 \pm 3 \text{ nm}$ ) film/the PMMA film ( $M_w = 15 \text{ kg mol}^{-1}$ , different film thickness)/the Si wafer with 120 nm oxide layer was treated at  $160^\circ\text{C}$ . (a)–(c) a series of OM images show the morphology of the liquid-gas interface; (d)–(f) a series of AFM images show the morphology of the polymer/polymer interface after the PS upper layer is removed. The scale of bar in (a)–(c) is  $10 \mu\text{m}$ .



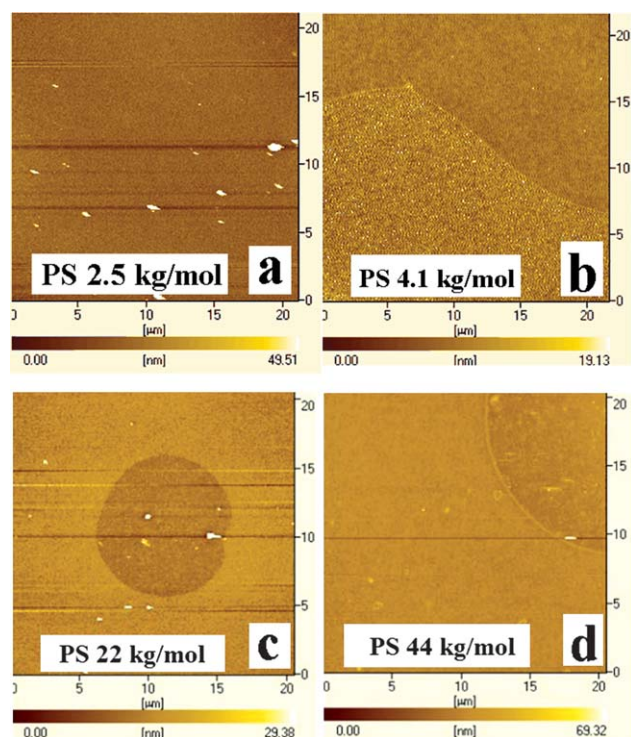


**Fig. 7** The PS film/the PMMA film ( $M_w = 365 \text{ kg mol}^{-1}$ , different film thickness)/the Si wafer with 120 nm oxide layer was treated at  $160^\circ\text{C}$ . A series of OM images show the morphology of the liquid-gas interface. (a)–(c): PS ( $M_w = 2.5 \text{ kg mol}^{-1}$ ,  $h_U = 65 \pm 3 \text{ nm}$ ) film; (d)–(f): PS ( $M_w = 4.1 \text{ kg mol}^{-1}$ ,  $h_U = 65 \pm 3 \text{ nm}$ ) film; (g)–(i): PS ( $M_w = 22 \text{ kg mol}^{-1}$ ,  $h_U = 65 \pm 3 \text{ nm}$ ) film; (j)–(l): PS ( $M_w = 44 \text{ kg mol}^{-1}$ ,  $h_U = 65 \pm 3 \text{ nm}$ ) film. The scale of bar in Figure 7 is  $10 \mu\text{m}$ .

polymer/air interface because of the lower deformability of the polymer/polymer interface due to stronger van der Waals repulsion and viscous resistance. However, with increase in the lower layer thickness, the reduced van der Waals repulsion and smaller viscous resistance makes the polymer/polymer interface more unstable. The switchover takes place exactly at the point of discontinuity. The result is consistent with the previously found experimental observations. Curves 2–4 represent a scenario where both the layers are thermodynamically unstable. The left part of the plots shows that the instability is dictated by the rupture of an ultrathin lower layer. However, as the lower layer thickness is increased the destabilizing influence at the lower layer reduces and the upper layer becomes relatively more unstable. Thus, the dominant mode of instability shifts to the polymer/air interface. With further increase in the lower layer

thickness the smaller viscous resistance at the lower layer increases the deformability of the polymer/polymer interface and the instability evolves by the upper layer rupture with larger deformation at the polymer/polymer interface. The plots also show that the shifts of instabilities from one interface to other take place exactly at the locations of the discontinuities as shown in the curve 2. Curves 3 and 4 confirm that the switchover prevails even when the bilayer rests on higher energy surfaces. Curve 5 shows the results for a same system considered in curve 2 but with increased viscosity at the upper layer. The curve confirms that increase in the viscosity of the upper layer binds the interfaces better, which helps the dominant mode to stay at the polymer/polymer interface and evolve at a single wavelength. In the left (right) side of the minimum of curve 5 in Fig. 10c the lower (upper) layer ruptures. Fig. 10d clarifies that in such

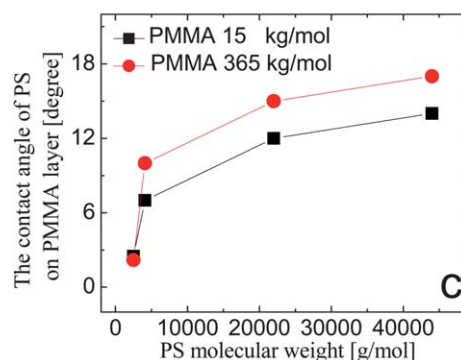
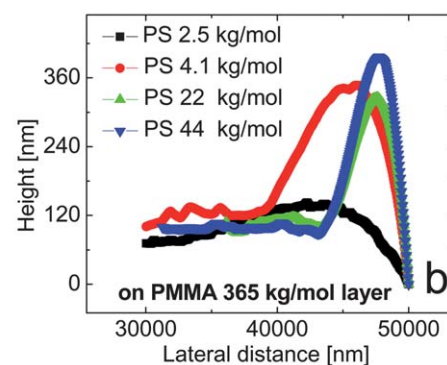
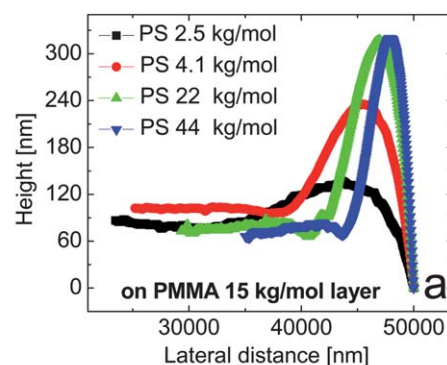




**Fig. 8** The PS film ( $65 \pm 3$  nm)/the PMMA film ( $M_w = 365$  kg mol $^{-1}$ , 190 nm)/the Si wafer with 120 nm oxide layer was treated at 160 °C. After the PS upper layer is removed, a series of AFM images show the morphology of the polymer/polymer interface. (a): PS ( $M_w = 2.5$  kg mol $^{-1}$ ) film; (b): PS ( $M_w = 4.1$  kg mol $^{-1}$ ) film; (c): PS ( $M_w = 22$  kg mol $^{-1}$ ) film; (d): PS ( $M_w = 44$  kg mol $^{-1}$ ) film.

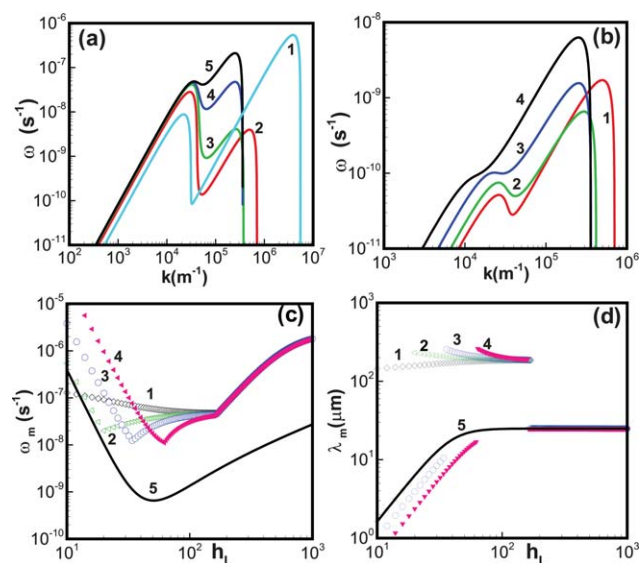
situations the larger wavenumber maximum always remains the dominant mode with the change in the lower layer thickness. The lower stabilizing interfacial tension plays key role here to ensure the larger deformability and hence the dominant mode to stay always at the polymer/polymer interface. Fig. 11 shows that for a bilayer when the film thicknesses are constant, the growth of instability and corresponding wavelength can be shifted from one interface to the other by changing the ratio of viscosities of the films. Again, the points of discontinuities are the regions where dominant mode of instability shifts from polymer/air to polymer/polymer interface or *vice versa*. The smaller (larger) wavelength maxima here correspond to the polymer/polymer (polymer/air) interface.

Fig. 12 shows the spatiotemporal evolution of the interfaces which qualitatively explains the experimentally found dewetting mechanisms. Fig. 12a shows that when the lower layer is of higher viscosity and smaller thickness the dominant mode of instability deforms the polymer/air interface more significantly and the holes are formed at the upper layer owing to the stronger destabilizing intermolecular interactions at the upper layer. The simulations undoubtedly demonstrate that this has been the mechanism of dewetting as found in the experiments. Fig. 12b shows that when the lower layer thickness is further increased the interfaces now evolve with two different wavelengths in the nonlinear regime of the evolution. Thus, the polymer/polymer interface is found to form a larger number of columnar structures under the hole-floor formed by the upper



**Fig. 9** The profile images of the rim (a) on PMMA film ( $M_w = 15$  kg mol $^{-1}$ , the film thickness  $h = 10$  nm); (b) on PMMA film ( $M_w = 365$  kg mol $^{-1}$ , the film thickness  $h = 11$  nm); (c) the plot of the receding contact angle and PS molecular weight.

layer (curve 3). The simulation resembles the experiments where the PS layer invades into the PMMA layer under the hole-floor of the PS upper layer as shown in the Fig. 2. It is important to note here that although  $\omega$  vs.  $k$  plots show for bimodal behavior for both the Fig. 12a and 12b, it is only the system shown in Fig. 12b evolves with a two different wavelengths at the interfaces even in the nonlinear regime. In case of Fig. 12a, although the instability starts with two different wavelengths at the interfaces but later the nonlinear forces take over and both the interfaces again evolve with a single wavelength in the late stages of dewetting. Fig. 12c shows the other dewetting scenario, where the instability is dictated by the rupture of upper layer



**Fig. 10** The plots display the results from the linear stability analysis (LSA). Plot (a) shows the variation of the linear growth coefficient ( $\omega$ ) with the wave number ( $k$ ) when  $\mu_2 = 100$  Pa s and  $\mu_1 = 10^5$  Pa s and plot (b) show the same when  $\mu_1 = \mu_2 = 10^5$  Pa s. Curves 1–5 in plot (a) correspond to 10 nm, 30 nm, 70 nm, 170 nm, and 290 nm thick lower layers, respectively. Curves 1–4 in plot (b) correspond to 50 nm, 110 nm, 190 nm, and 290 nm thick lower layers, respectively. Plots (c) and (d) show the variations of the dominant growth rate ( $\omega_m$ ) and wavelength ( $\lambda_m$ ) with the change in the lower layer thickness ( $h_L$ ). The curves 1–4 in these plots represent substrate surface energies 20 mN m<sup>-1</sup>, 40 mN m<sup>-1</sup>, 60 mN m<sup>-1</sup> and 120 mN m<sup>-1</sup>, respectively, when  $\mu_2 = 100$  Pa s and  $\mu_1 = 10^5$  Pa s. Curve 5 shows when  $\mu_2 = \mu_1 = 10^5$  Pa s and when the substrate surface energy is 40 mN m<sup>-1</sup>. In upper layer thickness is kept constant at 65 nm.

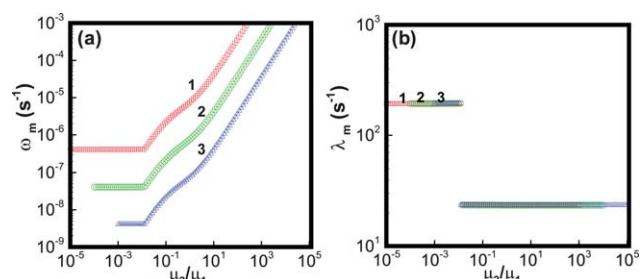


**Fig. 11** The plots display the results from the linear stability analysis (LSA). Plots (a) and (b) show the variations of the dominant growth rate ( $\omega_m$ ) and wavelength ( $\lambda_m$ ) with the change in the viscosity ratio ( $\mu_2/\mu_1$ ). The curves 1–3 in these plots represent  $\mu_2 = 10$  Pa s, 100 Pa s, and 1000 Pa s, respectively. Other parameters are  $\gamma_S = 40$  mN m<sup>-1</sup>, upper and lower layer thicknesses are kept constant at 10 nm and 65 nm.

due to larger deformation at the polymer/polymer interface. In such a situation, the upper layer ‘penetrates’ into the lower layer near the three phase contact line because of the lower viscous resistance at the thicker lower layers. The simulation closely resembles the experimentally found trench formation under similar conditions. Interestingly, the bilayers with larger viscosity at the upper layer follow a similar pathway of dewetting as found in Fig. 12c.

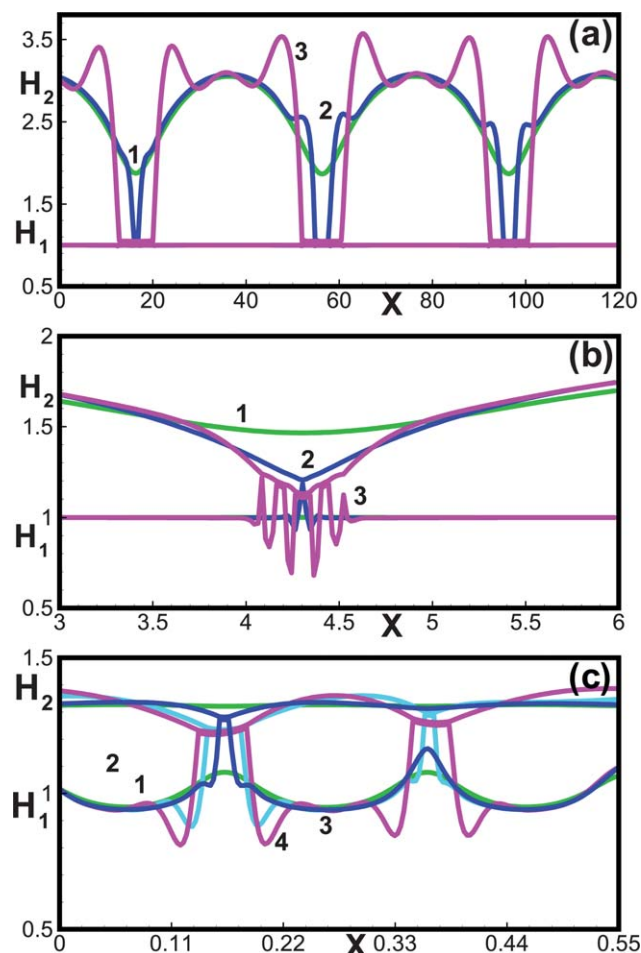


**Fig. 12** Spatiotemporal evolution of thin viscous bilayers. Curves 1–3 in plot (a) show the deformations at the interfaces at (1)  $T = 0.1267$ , (2),  $T = 0.127$ , and (3)  $T = 0.1271$ , when  $h_1 = h_L = 40$  nm and  $h_2 = h_L + h_U = 105$  nm. Curves 1–3 in plot (b) show the deformations at the interfaces at (1)  $T = 0.00094$ , (2)  $T = 0.000954$ , and (3)  $T = 0.000955$ . Curves 1–4 in plot (c) show the deformations at the interfaces at (1)  $T = 1.63 \times 10^{-5}$ , (2),  $T = 1.65 \times 10^{-5}$ , (3)  $T = 1.654 \times 10^{-5}$ , and (4)  $T = 1.655 \times 10^{-5}$ . In the simulations  $\mu_2 = 100$  Pa s,  $\mu_1 = 10^5$  Pa s,  $\gamma_2 = 40$  mN m<sup>-1</sup>,  $\gamma_1 = 30$  mN m<sup>-1</sup>, and  $\gamma_S = 40$  mN m<sup>-1</sup>.

## 5. Conclusions

The kinetically controlled instabilities of ultrathin bilayers and subsequent interfacial morphologies are investigated employing a PS/PMMA bilayer on a Si substrate with 120 nm thick oxide layer. The instabilities are engendered by the intermolecular forces and have shown a number of interesting features when the kinetic forces such as viscosities of the layers are tuned. Experiments together with theoretical computations have identified the location of the dominant mode of instability under varied conditions. The kinetic forces are made prominent by changing the molecular weight the PS layer and the film thickness and molecular weight of the PMMA layer. The molecular weight eventually changes the viscosity of the film and thus redistributes the strength of the intermolecular interactions in the polymer layers during the spatiotemporal interfacial evolution. A thin or high viscosity PMMA lower layer is found to be kinetically stable

and PS dewets on the non-deforming PMMA like a single film, which ensures that larger deformability at the polymer/air interface. In contrast, on the low  $M_w$  PMMA ( $M_w = 15 \text{ kg mol}^{-1}$ ), with the increase in the lower PMMA layer, the dominant mode of interfacial instability shifts from polymer/air interface to polymer/polymer interface. Besides, on a thick PMMA ( $M_w = 15 \text{ kg mol}^{-1}$ ) lower layer, larger deformability at the polymer/polymer interface shifts the dominant mode of instability exclusively to the polymer/polymer interface when the PS film is of low viscosity ( $M_w = 2.5 \text{ kg mol}^{-1}$ ). Interestingly, at intermediate thicknesses the interfaces are found to evolve in two different wavelengths and the upper layer tend to invade locally into the lower layer under the hole-floor of the PS upper layer on the PMMA layer. It is important to note that when the PS layer is of higher viscosity ( $M_w = 4.1 \text{ kg mol}^{-1}$ ,  $M_w = 22 \text{ kg mol}^{-1}$  and  $M_w = 44 \text{ kg mol}^{-1}$ ) these transitions are found to be absent.

## Acknowledgements

This work is supported by the World Class University Grant No. R32-2008-000-20082-0 of the National Research Foundation of Korea.

## References

- 1 E. Ruckenstein and R. K. Jain, *J. Chem. Soc., Faraday Trans. 2*, 1974, **70**, 132–147.
- 2 P. G. De Gennes, *Rev. Mod. Phys.*, 1985, **57**, 827–863.
- 3 C. Redon, F. Brochard-Wyart and F. Rondelez, *Phys. Rev. Lett.*, 1991, **66**, 715–718.
- 4 G. Reiter, *Phys. Rev. Lett.*, 1992, **68**, 75–78.
- 5 A. Sharma, *Langmuir*, 1993, **9**, 861–869.
- 6 G. Reiter, *Langmuir*, 1993, **9**, 1344–1351.
- 7 A. Oron, S. H. Davis and S. G. Bankoff, *Rev. Mod. Phys.*, 1997, **69**, 931–980.
- 8 K. Jacobs, R. Seemann, G. Schatz and S. Herminghaus, *Langmuir*, 1998, **14**, 4961–4963.
- 9 A. Sharma and R. Khanna, *Phys. Rev. Lett.*, 1998, **81**, 3463–3466.
- 10 A. Oron and S. G. Bankoff, *J. Colloid Interface Sci.*, 1999, **218**, 152–166.
- 11 P. Müller-Buschbaum, J. S. Gutmann, M. Stamm, R. Cubitt, S. Cunis, G. von Krosigk, R. Gehrke and W. Petry, *Phys. B*, 2000, **283**, 53–59.
- 12 U. Thiele, M. Velarde and K. Neuffer, *Phys. Rev. Lett.*, 2001, **87**, 016104.
- 13 J.-L. Masson and P. F. Green, *Phys. Rev. Lett.*, 2002, **88**, 205504–1.
- 14 H. Kaya and B. Jérôme, *Eur. Phys. J. E*, 2003, **12**, 383–388.
- 15 M. Geoghegan and G. Krausch, *Prog. Polym. Sci.*, 2003, **28**, 261–302.
- 16 J. Becker, G. Grün, R. Seemann, H. Mantz, K. Jacobs, K. Mecke and A. Blossey, *Nat. Mater.*, 2002, **2**, 59–63.
- 17 L. M. Pismen, *Phys. Rev. E: Stat., Nonlinear, Soft Matter Phys.*, 2004, **70**, 021601.
- 18 M. D. Morariu, E. Schäffer and U. Steiner, *Phys. Rev. Lett.*, 2004, **92**, 156102.
- 19 G. Narsimhan, *J. Colloid Interface Sci.*, 2005, **287**, 624–633.
- 20 V. Mitlin, *J. Colloid Interface Sci.*, 2005, **281**, 444–448.
- 21 O. Baumchen, R. Fetzer and K. Jacobs, *Phys. Rev. Lett.*, 2009, **103**, 247801.
- 22 S. Gabriele, P. Damman, S. Slavovs, S. Desprez, S. Coppée, G. Reiter, M. Hamieh, S. A. Akhrass, T. Vilmin and E. Raphaël, *J. Polym. Sci., Part B: Polym. Phys.*, 2006, **44**, 3022–3030.
- 23 M. Hamieh, S. A. Akhrass, T. Hamieh, P. Damman, S. Gabriele, T. Vilmin, E. Raphaël and G. Reiter, *J. Adhes.*, 2007, **83**, 367–381.
- 24 L. Xu, T. F. Shi, P. K. Dutta and L. J. An, *J. Chem. Phys.*, 2007, **127**, 144704.
- 25 L. Xu, T. F. Shi and L. J. An, *Langmuir*, 2007, **23**, 9282–9286.
- 26 L. Xu, X. F. Yu, T. F. Shi and L. J. An, *Soft Matter*, 2009, **5**, 2109–2116.
- 27 M. H. Yang, S. Y. Hou, Y. L. Chang and A. C.-M. Yang, *Phys. Rev. Lett.*, 2006, **96**, 066105.
- 28 B. K. Yoon, J. Huh, H.-C. Kim, J.-M. Hong and C. Park, *Macromolecules*, 2006, **39**, 901–903.
- 29 S. A. Burke, J. M. Topple and P. Grutter, *J. Phys.: Condens. Matter*, 2009, **21**, 423101.
- 30 G. Reiter, P. Auroy and L. Auvray, *Macromolecules*, 1996, **29**, 2150–2157.
- 31 R. Xie, A. Karim, J. F. Douglas, C. C. Han and R. A. Weiss, *Phys. Rev. Lett.*, 1998, **81**, 1251–1254.
- 32 R. Konnur, K. Kargupta and A. Sharma, *Phys. Rev. Lett.*, 2000, **84**, 931–934.
- 33 K. Kargupta and A. Sharma, *Phys. Rev. Lett.*, 2001, **86**, 4536–4539.
- 34 A. Sehgal, V. Ferreiro, J. F. Douglas, E. J. Amis and A. Karim, *Langmuir*, 2002, **18**, 7041–7048.
- 35 K. Kargupta and A. Sharma, *J. Colloid Interface Sci.*, 2002, **245**, 99–115.
- 36 L. Brusch, H. Kühne, U. Thiele and M. Bär, *Phys. Rev. E: Stat. Phys., Plasmas, Fluids, Relat. Interdiscip. Top.*, 2002, **66**, 011602.
- 37 K. Kargupta and A. Sharma, *Langmuir*, 2003, **19**, 5153–5163.
- 38 O. Wunnicke, P. Müller-Buschbaum, M. Wolkenhauer, C. Lorenz-Haas, R. Cubitt, V. Leiner and M. Stamm, *Langmuir*, 2003, **19**, 8511–8520.
- 39 U. Thiele, L. Brusch, M. Bestehorn and M. Bär, *Eur. Phys. J. E*, 2003, **11**, 255–271.
- 40 D. Juthongpipit, W. H. Zhang, J. F. Douglas, A. Karim and M. J. Fasolka, *Soft Matter*, 2007, **3**, 613–618.
- 41 R. Mukherjee, D. Bandyopadhyay and A. Sharma, *Soft Matter*, 2008, **4**, 2086–2097.
- 42 S. H. Kim, M. J. Misner and T. P. Russell, *Adv. Mater.*, 2004, **16**, 2119–2123.
- 43 S. Manigandan, S. Majumder, A. Suresh, S. Ganguly, K. Kargupta and D. Banerjee, *Sens. Actuators, B*, 2010, **144**, 170–175.
- 44 H. Yoneda, Y. Nishimura, Y. Doi, M. Fukuda and M. Kohno, *Polym. J.*, 2010, **42**, 425–437.
- 45 K. Nakata, T. Kobayashi and E. Tokunaga, *Opt. Rev.*, 2010, **17**, 346–351.
- 46 X. Wang, S. Yakovlev, K. M. Beers, M. J. Park, S. A. Mullin, K. H. Downing and N. N. Balsara, *Macromolecules*, 2010, **43**, 5306–5314.
- 47 M. Eguilaz, L. Aguei, P. Yanez-Sedeno and J. M. Pingarron, *J. Electroanal. Chem.*, 2010, **644**, 30–35.
- 48 H. Ogawa, T. Kanaya, K. Nishida, G. Matsuba, J. P. Majewski and E. Watkins, *J. Chem. Phys.*, 2009, **131**, 104907.
- 49 C. Neto, M. James and A. M. Telford, *Macromolecules*, 2009, **42**, 4801–4808.
- 50 H.-j. Chung, K. Ohno, T. Fukuda and R. J. Composto, *Macromolecules*, 2007, **40**, 384–388.
- 51 Y. Liao, Z. Su, Z. Sun, T. Shi and L. An, *Macromol. Rapid Commun.*, 2006, **27**, 351–355.
- 52 Z. Lin, T. Kerle, T. P. Russell, E. Schäffer and U. Steiner, *Macromolecules*, 2002, **35**, 3971–3976.
- 53 D. C. Abeysinghe, W. B. Chen, Q. W. Zhan and R. E. Nelson, *Nanotechnology*, 2009, **20**, 475301.
- 54 B. Kim, D. Y. Ryu, V. Pryamitsyn and V. Ganesan, *Macromolecules*, 2009, **42**, 7919–7923.
- 55 G. Lee, B. Yoon, H. Acharya, C. Park and J. Huh, *Macromol. Res.*, 2009, **17**, 181–186.
- 56 A. P. Siegel, M. J. Murcia, M. Johnson, M. Reif, R. Jordan, J. Ruhe and C. A. Naumann, *Soft Matter*, 2010, **6**, 2723–2732.
- 57 Y. P. Wang, P. Han, G. L. Wu, H. P. Xu, Z. Q. Wang and X. Zhang, *Langmuir*, 2010, **26**, 9736–9741.
- 58 A. Sandstrom, P. Matyba, O. Inganas and L. Edman, *J. Am. Chem. Soc.*, 2010, **132**, 6646–6647.
- 59 B. J. Park, J. N. Park, J. S. Choi and H. J. Choi, *J. Nanosci. Nanotechnol.*, 2010, **10**, 4758–4761.
- 60 J. Gomez, F. Sagues and R. Reigada, *J. Chem. Phys.*, 2010, **132**, 135104.
- 61 J. H. Huang, K. C. Li, D. Kekuda, H. H. Padhy, H. C. Lin, K. C. Ho and C. W. Chu, *J. Mater. Chem.*, 2010, **20**, 3295–3300.
- 62 F. Brochard-Wyart, P. Martin and C. Redon, *Langmuir*, 1993, **9**, 3682–3690.
- 63 M. Sferrazza, M. Heppenstall-Butler, R. Cubitt, D. G. Bucknall, J. Webster and R. A. L. Jones, *Phys. Rev. Lett.*, 1998, **81**, 5173–5176.
- 64 P. Lambooy, K. C. Phelan, O. Haugg and G. Krausch, *Phys. Rev. Lett.*, 1996, **76**, 1110–1113.



- 65 L. Xu, X. F. Yu, T. F. Shi and L. J. An, *Macromolecules*, 2008, **41**, 21–24.
- 66 L. Xu, T. F. Shi and L. J. An, *J. Chem. Phys.*, 2009, **130**, 184903.
- 67 L. Xu, G. Reiter, T. F. Shi and L. J. An, *Langmuir*, 2010, **26**, 7270–7276.
- 68 J. P. de Silva, M. Geoghegan, A. M. Higgins, G. Krausch, M.-O. David and G. Reiter, *Phys. Rev. Lett.*, 2007, **98**, 267802.
- 69 S. Al Akhrass, G. Reiter, S. Y. Hou, M. H. Yang, Y. L. Chang, F. C. Chang, C. F. Wang and A. C.-M. Yang, *Phys. Rev. Lett.*, 2008, **100**, 178301.
- 70 B. M. Besancon and P. F. Green, *J. Chem. Phys.*, 2007, **126**, 224903.
- 71 K. D. Danov, V. N. Paunov, N. Alleborn, H. Raschler and F. Durst, *Chem. Eng. Sci.*, 1998, **53**, 2809–2822.
- 72 K. D. Danov, V. N. Paunov, S. D. Stoyanov, N. Alleborn, H. Raschler and F. Durst, *Chem. Eng. Sci.*, 1998, **53**, 2823–2837.
- 73 V. N. Paunov, K. D. Danov, N. Alleborn, H. Raschler and F. Durst, *Chem. Eng. Sci.*, 1998, **53**, 2839–2857.
- 74 A. Pototsky, M. Bestehorn, D. Merkt and U. Thiele, *Phys. Rev. E: Stat., Nonlinear, Soft Matter Phys.*, 2004, **70**, 025201.
- 75 A. Pototsky, M. Bestehorn, D. Merkt and U. Thiele, *J. Chem. Phys.*, 2005, **122**, 224711.
- 76 A. Pototsky, M. Bestehorn, D. Merkt and U. Thiele, *Europhys. Lett.*, 2006, **74**, 665–671.
- 77 D. Bandyopadhyay, R. Gulabani and A. Sharma, *Ind. Eng. Chem. Res.*, 2005, **44**, 1259–1272.
- 78 D. Bandyopadhyay and A. Sharma, *J. Chem. Phys.*, 2006, **125**, 054711.
- 79 D. Bandyopadhyay and A. Sharma, *J. Phys. Chem. B*, 2008, **112**, 11564–11572.
- 80 D. Bandyopadhyay, A. Sharma and C. Rastogi, *Langmuir*, 2008, **24**, 14048–14058.
- 81 D. Bandyopadhyay and A. Sharma, *J. Phys. Chem. C*, 2010, **114**, 2237–2247.
- 82 L. S. Fisher and A. A. Golovin, *J. Colloid Interface Sci.*, 2007, **307**, 203–214.
- 83 A. A. Nepomnyashchy and I. B. Simanovskii, *Phys. Fluids*, 2006, **18**, 112101.
- 84 A. A. Nepomnyashchy and I. B. Simanovskii, *Phys. Fluids*, 2006, **18**, 032105.
- 85 A. A. Nepomnyashchy and I. B. Simanovskii, *Phys. Rev. Lett.*, 2009, **102**, 164501.
- 86 S. Kumar and O. K. Matar, *J. Colloid Interface Sci.*, 2004, **273**, 581.
- 87 O. K. Matar, V. Ckanis and S. Kumar, *J. Colloid Interface Sci.*, 2005, **286**, 319–332.
- 88 J. N. Israelachvili, *Intermolecular and Surface Forces*, Academic Press, London, 1992.
- 89 C. J. van Oss, M. K. Chaudhury and R. J. Good, *Chem. Rev.*, 1988, **88**, 927–941.
- 90 K. Fuchs, C. Friedrich and J. Weese, *Macromolecules*, 1996, **29**, 5893–5901.